Synthesis of Monophasic $Ca_xBa_{(1-x)}TiO_3$ Nanoparticles with High Ca Content ($x > 23\%$) and Their Photoluminescence Properties

Agus Purwanto,[†,‡] Darmawan Hidayat,[†] Yoshitake Terashi,[†,§] and Kikuo Okuyama*,[†]

Department of Chemical Engineering, Graduate School of Engineering, Hiroshima University, 1-4-1 Kagamiyama, Higashi Hiroshima, Hiroshima 739-8527, Japan, Department of Chemical Engineering, Faculty of Engineering, Sebelas Maret University, Jl. Ir. Sutami 36 A, Surakarta, Central Java 57126, Indonesia, and R&D Center, Kyocera Corporation, 1-4 Yamashita-Cho, Kokubu, Kagoshima 899-4312, Japan

Received September 17, 2008. Revised Manuscript Received October 27, 2008

We report for the first time the fabrication of monophasic $Ca_xBa_{(1-x)}TiO_3$ nanoparticles with high Ca content using a flame assisted spray pyrolysis (FASP) method. The biphasic structure (mixture of tetragonal $BaTiO_3$ and orthorhombic $CaTiO_3$ phases) was not detected in nanoparticles where $x > 23\%$. The as-prepared nanoparticles were spherical, nonagglomerated, and polycrystalline with a relatively narrow size distribution ($\sigma_g = 1.23 - 1.28$). STEM-EDS mapping revealed that all components (Ca, Ba, Ti) were homogeneously distributed inside the nanoparticles. The optical properties were evaluated by doping of $Ca_xBa_{(1-x)}TiO_3$ nanoparticles with Pr^{3+} ions. $Ca_xBa_{(1-x)}TiO_3$:Pr^{3+} nanophosphors exhibited an intense red emission at a wavelength of 612 nm. Interestingly, the excitation-wavelength peaks varied over the range of 323.2 to 354.2 nm by variation of x.

1. Introduction

Pr-doped $CaTiO_3$ is an important phosphor for low voltage field emission displays.[1,2] Development of $CaTiO_3$-based phosphors was initiated by the synthesis of Pr-doped $CaTiO_3$ phosphors reported by Diallo et al.[3] The intense red emission under UV excitation was ascribed to $4f^2-4f^2$ transition of Pr^{3+} ions from the excited state, $^1D_2$, to the ground state, $^3H_4$.[3−5] The addition of Ba ions to $CaTiO_3$:Pr^{3+} controlled, to some extent, the optical properties of $CaTiO_3$:Pr^{3+}.[1,2] Reportedly, the $(Ca_{0.23}Ba_{0.77})TiO_3$:$Pr^{3+}$ system has two emission peaks (at 490 and 611 nm) that have different intensities, depending on their crystal structure composition. This finding suggests that Pr^{3+}-doped $(Ca_{0.23}Ba_{0.77})TiO_3$ can be used as a structural probe to determine the phase transition in ceramics.[1] Recently, $(Ca_{0.23}Ba_{0.77})TiO_3$:$Pr^{3+}$ was shown to have interactions among its electrical, mechanical, and photon-emission properties.[6,7] When material was pressed or electrically charged, a red light was emitted, which would be useful for smart-skin and self-diagnostic application. In both reports, the phosphor was made of low Ca concentration (≤23%). A phosphor with Ca > 90% has been reported in the fabrication of $Ca_{1-x-y}Sr_xBa_yTiO_3$:Pr^{3+} ($x = 0.1-0.35$; $y = 0-0.09$). The addition of Ba to $Ca_{1-x-y}Sr_xBa_yTiO_3$ resulted in an excitation spectrum with a shoulderless peak at approximately 365 nm, as observed for $CaTiO_3$:Pr^{3+}.[2] However, the study of $Ca_xBa_{(1-x)}TiO_3$:Pr^{3+} phosphor that recorded a Ca content ranging from 23% to 90% cannot be found in the literature due to the lack of a processing procedure to prepare the solid solution in such a range. Thus, the present investigation focused on the fabrication of a $Ca_xBa_{(1-x)}TiO_3$:Pr^{3+} phosphor for $23\% < x < 90\%$. It is expected that the prepared phosphor will have photoluminescence behaviors that differ significantly from the already known Ca content.

The major difficulty encountered in the preparation of high-Ca $Ca_xBa_{(1-x)}TiO_3$ ($x > 23\%$) is the ready formation of biphasic structures of tetragonal $BaTiO_3$ and orthorhombic $CaTiO_3$. The literature indicates that the $Ca_xBa_{(1-x)}TiO_3$ solid solution exists only when $x \leq 23\%$; meanwhile, a fully orthorhombic phase exists when $x > 90\%$.[8−11] For x ranging from 23% to 90%, biphasic structures of tetragonal $BaTiO_3$ and orthorhombic $CaTiO_3$ were observed. The speculation was that these structures arose from imperfect homogeneity due to incomplete diffusion of Ca into $BaTiO_3$. This explanation is plausible because in the conventional method $(Ca,Ba)TiO_3$ particles are prepared by deposition of either Ca-containing compounds or a $CaTiO_3$ layer onto the surface of $BaTiO_3$ particles, which results in the formation of the

---

* To whom correspondence should be addressed: E-mail: Okuyama@hiroshima-u.ac.jp. Tel: +81-82-424-7716. Fax: +81-82-424-5494.

[†] Hiroshima University.

[‡] Sebelas Maret University.

[§] Kyocera Corporation.

(1) Zhang, P.; Shen, M.; Fang, L.; Zheng, F.; Wu, X.; Shen, J.; Chen, H. *Appl. Phys. Lett.* **2008**, *92*, 222908–1.

(2) Kyomen, T.; Sakamoto, R.; Sakamoto, N.; Kunugi, S.; Itoh, M. *Chem. Mater.* **2005**, *17*, 3200.

(3) Diallo, P. T.; Boutinaud, P.; Mahiou, R.; Cousseins, J. C. *Phys. Status Solidi A* **1997**, *160*, 255.

(4) Diallo, P. T.; Jeanlouis, K.; Boutinaud, P.; Mahiou, R.; Cousseins, J. C. *J. Alloys Compd.* **2001**, *323*, 218.

(5) Zhang, X.; Zhang, J.; Jin, Y.; Zhao, H.; Wang, X. J. *Cryst. Growth Des.* **2008**, *8*, 779.

(6) Wang, X. S.; Xu, C. N.; Yamada, H.; Nishikubo, K.; Zheng, X. G. *Adv. Mater.* **2005**, *17*, 1254.

(7) Wang, X. S.; Yamada, H.; Xu, C. N. *Appl. Phys. Lett.* **2005**, *86*, 022905–1.

(8) Cheng, X. R.; Shen, M. R. *Mater. Res. Bull.* **2007**, *42*, 1662.

(9) Sakabe, Y.; Wada, N.; Hiramatsu, T.; Tonogaki, T. *Jpn. J. Appl. Phys. 1* **2002**, *41*, 6922.

(10) Park, J. G.; Oh, T. S.; Kim, Y. H. *J. Mater. Sci.* **1992**, *27*, 5713.

(11) Cheng, X. R.; Shen, M. R. *Solid State Commun.* **2007**, *141*, 587.

10.1021/cm802524e CCC: $40.75 © 2008 American Chemical Society
Published on Web 11/21/2008

core−shell structure.[9] Addition of a Ca source in the solid state is also a commonly used method of $(Ca,Ba)TiO_3$ fabrication.[10,12] The solid state method requires high temperatures and long residence times to achieve completion of the reaction. If the process conditions are not sufficient to facilitate perfect diffusion of Ca ions into $BaTiO_3$, then biphasic structures result. In fact, to the best of our knowledge, fabrication of the monophasic structure $Ca_xBa_{(1-x)}TiO_3$ at $23\% < x < 90\%$ has not yet been reported. Therefore, preparation of monophasic $Ca_xBa_{(1-x)}TiO_3$ particles with an $x > 23\%$ remains to be a challenging area of research.

In this paper, we demonstrate the fabrication of monophasic $Ca_xBa_{(1-x)}TiO_3$ nanoparticles with an $x > 23\%$ using a flame-assisted spray pyrolysis (FASP) method. Using this technique, $Ca_xBa_{(1-x)}TiO_3$ nanoparticles were subjected to very high flame temperatures to achieve rapid reaction rates. In addition, intimate mixing of components in an aqueous precursor combined with a high reaction temperature within the flame ensured a perfect interdiffusion of Ba and Ca ions, which resulted in a monophasic structure. Then, Pr^{3+} ions were doped into $Ca_xBa_{(1-x)}TiO_3$ nanoparticles for any x value to investigate the effect of x (Ca content) on the photoluminescence (PL) properties.

2. Experimental Section

Preparation of $Ca_xBa_{(1-x)}TiO_3$ Nanoparticles. The experimental setup of the flame assisted spray pyrolysis (FASP) system has been described elsewhere.[13] The system consisted of an aerosol generator (ultrasonic nebulizer 1.7 MHz), a diffusion flame reactor, and a powder collector. The powder collector was a bag filter. A vacuum pump was used to move the particles to the bag filter. A condenser with a water-cooling system was used to condense the water vapor that was produced by methane combustion and solvent evaporation.

The precursor solution was made from $Ba(C_2H_3O_2)_2$ (99%), $Ca(NO_3)_2 \cdot 4H_2O$ (95.5%), $Ti(OCH(CH_3)_2)_4$ (titanium tetra isopropoxite (TTIP-97%)), and $Pr(NO_3)_3 \cdot 6H_2O$ (99.95%) that had been purchased from Kanto Chemicals (Tokyo, Japan) and used without further purification. The precursor concentration was varied from 0.05 to 0.2 M. To produce a transparent solution of TTIP, and approximately 30 mL of 1 N HNO_3 was added to the TTIP. The mixture was stirred vigorously for approximately 1 h to ensure complete mixing of the TTIP and HNO_3. $Ba(C_2H_3O_2)_2$ and $Ca(NO_3)_2 \cdot 4H_2O$ were added to produce the desired concentration. To produce $Ca_xBa_{(1-x)}TiO_3$-based phosphor, $Pr(NO_3)_3 \cdot 6H_2O$ was also added to the solution at a concentration 0.12 atom %.

The experiment was carried out by first atomizing the precursor solution using an ultrasonic nebulizer to produce droplets. Then, the droplets were transported to the flame zone using oxygen as the carrier gas at a flow rate of 4 L/min. The methane flow rate was 4 L/min, and the oxidant flow rate was 8.4 L/min. Under these conditions, the estimated maximum temperature of the flame is approximately 2500 °C based on the results of a FLUENT simulation.[14] Finally, the as-prepared particles were transported to the bag filter, collected, and then characterized.

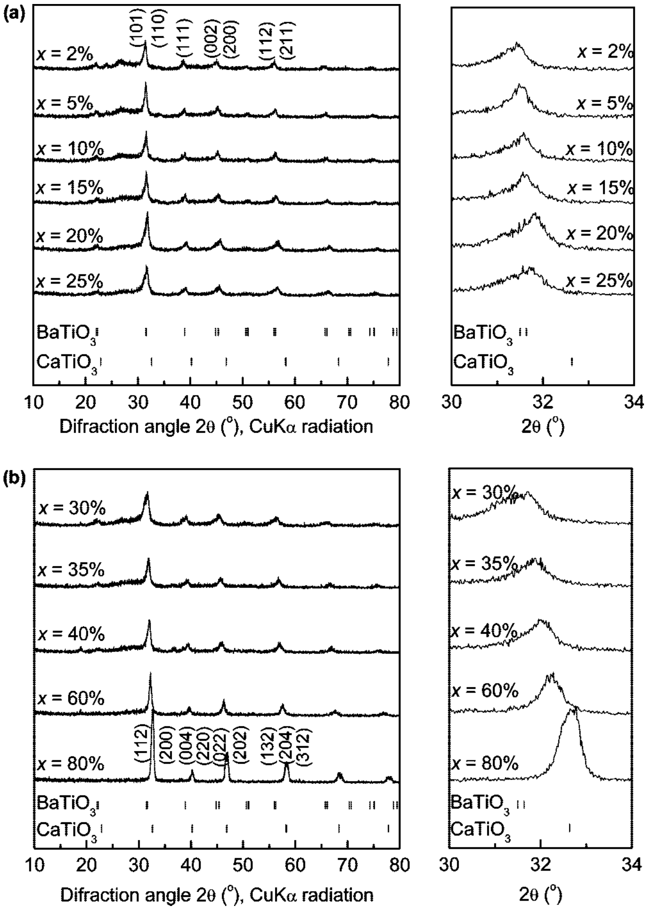

Figure 1. XRD patterns of $Ca_xBa_{(1-x)}TiO_3$ as a function of x. (a) The XRD pattern for $x \leq 25\%$ and (b) the XRD pattern for $x \geq 30\%$. Monophasic $Ca_xBa_{(1-x)}TiO_3$ was observed for all x values.

Table 1. Crystal Parameters of $Ca_xBa_{(1-x)}TiO_3$ Nanoparticles for Various x[a]

x (%)	a (Å)	b (Å)	c (Å)	V (Å^3)	crystal structure
2	4.0180	4.0180	4.0644	65.6160	tetragonal
5	3.9979	3.9979	4.0620	64.9234	tetragonal
10	3.9944	3.9944	4.0582	64.7498	tetragonal
20	3.9870	3.9870	4.0360	64.1569	tetragonal
25	3.9780	3.9780	4.0060	63.3929	tetragonal
40	3.9558	3.9558	3.9815	62.3038	tetragonal
60	5.5211	5.5689	7.8116	240.1770	orthorhombic
80	5.4688	5.5141	7.7283	233.0517	orthorhombic
100	5.4575	5.5170	7.7138	232.2599	orthorhombic

[a] $Ca_xBa_{(1-x)}TiO_3$ nanoparticles for $x < 50\%$ were indexed using tetragonal $BaTiO_3$ (JCPDS no 31-0174), while $x > 50\%$ was indexed using orthorhombic $CaTiO_3$ (JCPDS no 82-0232). The Rietveld refinement was carried out using the MAUD software package.

Characterization. The morphology of the as-prepared particles was observed at 20 kV by field-emission scanning electron microscopy (FE-SEM, S-5000, Hitachi Ltd., Tokyo, Japan). Prior to the analysis, particles were ion-sputtered for 30 s (E-1010, Hitachi, Tokyo, Japan). The geometric mean diameter (GMD, d_g) and geometric standard deviation (GSD, σ_g) were calculated using the equations, $\log d_g = (\sum n \log d)/(\sum n)$ and $\log \sigma_g = \{\sum[n(\log d - \log d_g)^2/\sum n]\}^{1/2}$, respectively, where d was the particle size based on FE-SEM images of approximately 200 randomly chosen particles. The morphology and electron diffraction of the crystals were examined in detail by transmission electron microscopy (TEM, JEM-2010, JEOL Ltd., Tokyo, Japan) at 300 kV. The crystallinity of particles was determined using selected area electron diffraction (SAED) coupled with TEM. Elemental mapping and chemical

---

(12) Mitsui, T.; Westphal, W. B. *Phys. Rev.* **1961**, *124*, 1354.

(13) Purwanto, A.; Wang, W. N.; Lenggoro, I. W.; Okuyama, K. *J. Eur. Ceram. Soc.* **2007**, *27*, 4489.

(14) Purwanto, A.; Wang, W. N.; Ogi, T.; Lenggoro, I. W.; Tanabe, E.; Okuyama, K. *J. Alloys Compd.* **2008**, *463*, 350.

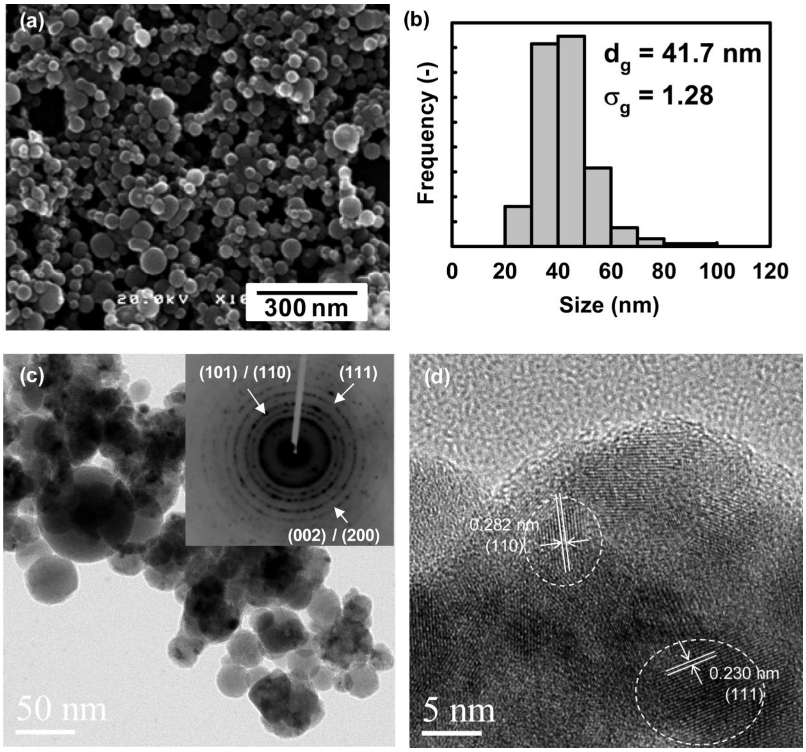

Figure 2. (a) FE-SEM, (b) size distribution, (c) TEM and diffraction pattern (inset), and (d) HR-TEM images of $Ca_xBa_{(1-x)}TiO_3$ ($x = 25\%$) nanoparticles. Nanoparticles were nonagglomerated, spherical, and polycrystalline with relatively narrow size distribution.

composition of particles were carried out using scanning transmission electron microscopy (STEM) equipped with energy dispersive X-ray spectroscopy (EDS). The chemical composition of the as-prepared nanoparticles was also analyzed using inductively coupled plasma mass spectrometry (ICP). Furthermore, the crystal structure of the powder was also examined using an X-ray diffractometer (XRD, RINT 2200V, Rigaku-Denki Corp., Tokyo, Japan). The XRD measurements were carried out using nickel-filtered Cu Kα (λ= 0.154 nm) at 40 kV and 30 mA with a scan step of 0.02° and a scan speed of 4°/min. To calculate the crystal parameters, Rietveld analysis was performed using a MAUD (material analysis using diffraction) software package.[15] The photoluminescence (PL) intensity was measured at an excitation wavelength of 330 nm using a xenon lamp. Meanwhile, PL excitation was measured at an emission wavelength of 612 nm. All optical spectra were measured at a resolution of 0.2 nm at room temperature.

3. Results and Discussion

As previously reported, in the $CaTiO_3-BaTiO_3$ system, a solid solution of $Ca_xBa_{(1-x)}TiO_3$ was observed only when $x \leq 23\%$.[8−12] It is worth noting that these prior studies used solid-state methods to prepare $Ca_xBa_{(1-x)}TiO_3$. When $x > 23\%$, a biphasic structure was produced, most likely due to the imperfect interdiffusion of precursor components. To address this issue, a flame assisted spray pyrolysis (FASP) method was investigated for the fabrication of $Ca_xBa_{(1-x)}TiO_3$ with a high Ca content ($x > 23\%$). FASP was selected because it offers better mixing of precursor components at the molecular level and high reaction temperatures result in rapid reaction rates, ensuring completion of reactions.

The phase transformation from tetragonal $BaTiO_3$ to orthorhombic $CaTiO_3$, as a function of x in the $Ca_xBa_{(1-x)}TiO_3$ system, is shown by two XRD patterns in Figure 1. The detailed XRD pattern of the as-prepared particles for $x < 25\%$ is shown in Figure 1a, while the higher value of x is shown in Figure 1b. In addition, to show the transition of strong diffraction peaks of tetragonal $BaTiO_3$ ((101) and (110) planes) and orthorhombic $CaTiO_3$ ((200) and (121) planes), XRD patterns for diffraction angle 2θ, ranging from 30 to 34°, are shown in Figure 1a,b. Both figures show that, at a low concentration of Ca ($x < 50\%$), the as-prepared $Ca_xBa_{(1-x)}TiO_3$ particles fit well with the tetragonal $BaTiO_3$ (Joint Committee for Powder Diffraction Standards, JCPDS no 31-0174, space group: *p*4*mm*). Meanwhile, the XRD patterns for $x > 50\%$ are consistent with orthorhombic $CaTiO_3$ (JCPDS no. 82-0232; space group, *pbnm*).[16,17] For a content of $x < 10\%$, broad peak was observed in the range of from 25° to 30°. This peak may represent an amorphous part in nanoparticles that gradually disappears with a high Ca content. It also is worth noting that insignificant diffraction peak around 18° was observed for $x = 40\%$ and 60%. This peak may be correlated with $Ba(NO_3)_2$ (JCPDS no 76-1376), which was produced from the reaction of high concentration NO_3 ions with Ba ions. On the basis of the strong diffraction peaks of 2θ from 30 to 34° (Figure 1b), it was evident that the positions of the diffraction peaks shifted upward as x increased. Interestingly, a biphasic structure of tetragonal $BaTiO_3$ and orthorhombic $CaTiO_3$ was not detected at any x value, indicating the

---

(15) Lutterotti, L.; Matthies, S.; Chateigner, D.; Ferrari, S.; Ricote, J. *Textures of Materials, ICOTOM 13, Proc. Int. Conf. 13th, Parts 1 and 2* **2002**, *1603*, 408-4.

(16) Liu, X.; Liebermann, R. C. *Phys. Chem. Miner.* **1993**, *20*, 171.

(17) Vashook, V.; Vasylechko, L.; Knapp, M.; Ullmann, H.; Guth, U. *J. Alloys Compd.* **2003**, *354*, 13.

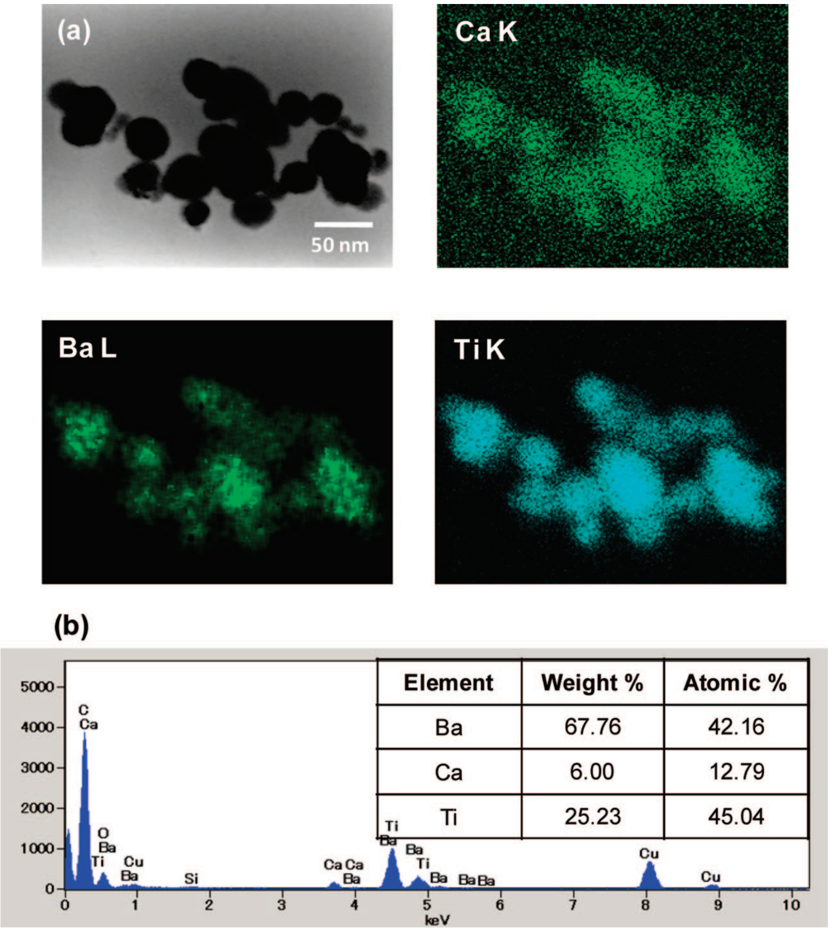

Element	Weight %	Atomic %
Ba	67.76	42.16
Ca	6.00	12.79
Ti	25.23	45.04

Figure 3. (a) Elemental mapping and (b) EDS spectra of $Ca_xBa_{(1-x)}TiO_3$ ($x = 25\%$). All components were well distributed inside the nanoparticles.

formation of a perfect solid solution of $Ca_xBa_{(1-x)}TiO_3$ particles. In addition, the unit cell parameters of $Ca_xBa_{(1-x)}TiO_3$ particles were analyzed using Rietveld refinement for all x values, as shown in Table 1. For $x < 50\%$ (tetragonal $BaTiO_3$), the unit cell constants, a and c, are decreased linearly by 1.71% and 1.08%, respectively. The same result was observed for the unit volume cell, which decreased linearly by 4.45%. For $x > 50\%$, the XRD pattern was refined using orthorhombic $CaTiO_3$. Compared with pure $CaTiO_3$, the addition of Ba ($x = 60\%$) improved a, b, c, and V by 1.16%, 0.94%, 1.27%, and 3.41%, respectively.

Morphology and size distribution of $Ca_xBa_{(1-x)}TiO_3$ particles for $x = 25\%$ were analyzed from FE-SEM and TEM images, as shown in Figure 2. Generally, the as-prepared particles are spherical, smooth in surface, and nonagglomerated. The geometric mean diameter of the particles was 41.7 nm (nanoparticles) with a geometric standard size distribution of 1.28 (Figure 2b). In addition, the precursor concentration could be used to control nanoparticle size. The geometric mean diameters of nanoparticles prepared from precursor concentrations of 0.05 M, 0.075 M, 0.1 M, and 0.2 M were 31.1 nm, 35.9 nm, 38.7 nm, and 41.7 nm, respectively. The geometric standard deviations ranged from 1.23 to 1.28, indicating that the as-prepared nanoparticles have a relatively narrow size distribution, regardless of size. The SAED spectra consisted of many diffraction rings, indicating that the nanoparticles were polycrystalline (Figure 2c, inset). This polycrystallinity is supported by high-resolution TEM (HR-TEM) imaging (Figure 2d), which shows that the nanoparticle consisted of numerous crystals with different lattice orientations. Results were similar to those described above were observed for the $Ca_xBa_{(1-x)}TiO_3$ nanoparticles where $x = 5\%$ (see Supporting Information).

To further evaluate the internal composition of the $Ca_xBa_{(1-x)}TiO_3$ ($x = 25\%$) nanoparticles, elemental mapping was conducted using STEM with EDS. The corresponding maps of calcium (Ca), barium (Ba), and titanium (Ti) are shown in Figure 3. A perfect distribution of the components (Ba, Ca, and Ti) was observed (Figure 3a); the elemental composition is shown in Figure 3b. Detailed compositional analysis was also carried out in a single nanoparticle in a five-positions analysis, as shown in Figure 4. Generally, the concentrations of Ca, Ba, and Ti at these points are relatively uniform. For information, the detail compositional analysis of $Ca_xBa_{(1-x)}TiO_3$ nanoparticles for $x = 20\%$ was also conducted (see Supporting Information). In addition, the composition was confirmed using the ICP method, as shown in Table 2. The composition of nanoparticles was very similar to that of the precursor composition, indicating no loss of components during preparation of the nanoparticles.

Thus, we successfully produced monophasic $Ca_xBa_{(1-x)}TiO_3$ nanoparticles with a high Ca content ($x > 23\%$) using the FASP method. To analyze solid-solution formation at a high Ca content ($x > 23\%$), simple solid-state kinetics were used. In a solid-state reaction, when reactants are in separate crystal lattices, the reaction rate is

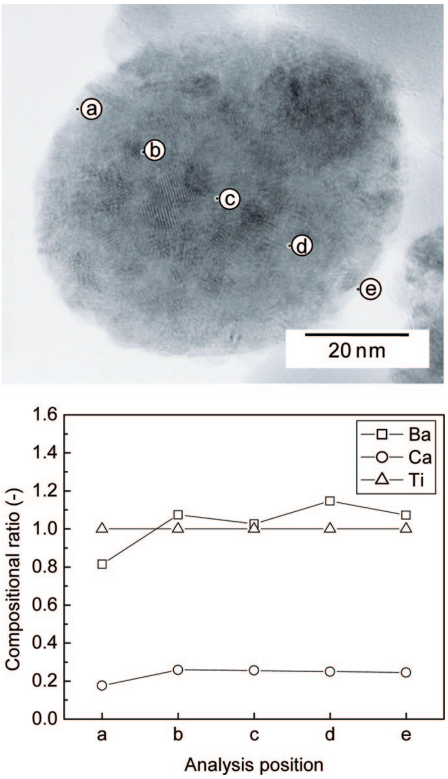

Figure 4. Compositional analysis of a single $Ca_xBa_{(1-x)}TiO_3$ ($x = 25\%$) nanoparticle. The composition distribution was relatively homogeneous inside the nanoparticle.

Table 2. ICP Analysis of $Ca_xBa_{(1-x)}TiO_3$ Powder

x (%)	Ba	Ca	Ti
10	0.9	0.09	1
20	0.81	0.19	1
25	0.73	0.24	1
30	0.69	0.3	1

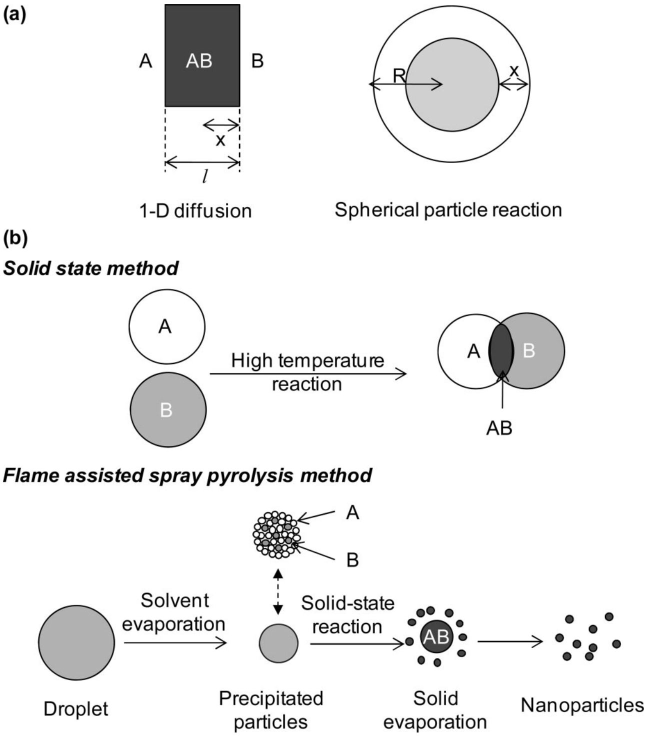

Figure 5. (a) One-dimensional diffusion through a flat plane (left) and schematic diagram for a spherical particle (right). A and B are reactants, AB is a reaction product, l is the thickness of the interface, x is the diffusion distance from the interface, and R is the radius of the particle. (b) Schematic diagram of the reaction mechanisms in solid-state (top) and flame-assisted spray pyrolysis (FASP) (bottom) methods.

controlled by diffusion: the rate of product formation decreases in proportion to the thickness of the product barrier. A simple schematic diagram of the solid-state reaction mechanism is presented in Figure 5a. In one-dimensional analysis, the formation rate of the product layer, AB, can be written as[18]

$$\frac{\mathrm{d}l}{\mathrm{d}t} = -D\frac{M_{AB}}{M_{B\rho}}\frac{\mathrm{d}C}{\mathrm{d}x} \tag{1}$$

where l is the thickness of the product layer, D is the diffusion constant, and M_{AB} and M_B are the molecular weight of AB and B, respectively. Applying three-dimensional analysis and using a spherical particle, A, as a model of the reactant (Figure 5a), the reaction rate of A and B, in which B (mass) moves across the interface (area) per unit of time to form product AB, can be solved as[18]

$$(1-(1-\alpha)^{1/3})^2 = k't \tag{2}$$

where

$$k' = k/R^2 \tag{3}$$

$$k = 2D[M_{AB}(C_2 - C_1)]/M_B p \tag{4}$$

α is a conversion fraction, k' is a constant, ρ is the density of the product (AB), and C is the concentration of B in AB. The concentration of B in AB is dependent on the thickness of AB; in a spherical system, the thickness of AB is referred to as R (radius) (Figure 5a). This equation is also known as the 3-D diffusion-Jander model.[18]

From the above equations, the rate of reaction was shown to be inversely proportional to R^2. For example, reducing the size of the particle by one-half will increase the reaction rate by four times its initial value. In the solid-state method, $Ca_xBa_{(1-x)}TiO_3$ was prepared from solid reactants using grinding or milling to mix the precursors.[9,12,19] Consequently, the size of the solid reactants is strongly dependent on the effectiveness of the grinding or milling process. Generally, the size of solid reactants ranges from submicrometer to micrometer order. As illustrated in Figure 5, completion of the reaction using the solid-state method would only be achieved after all components diffuse completely along the radius, R. By contrast, in the FASP method, particles were fabricated from droplets of a solution (approximately 4 μm in diameter). After drying was complete, the precipitated particles were submicrometer in size, depending on their precursor concentration (Figure 5b).[13] The precipitated particles act as a single reactor during a solid-state reaction, in which all components are already well-mixed.[13,20] The size of the precipitated reactant ranges from a single molecule to a few nanometers, depending on the nucleation conditions.[21,22]

---

(18) Khawam, A.; Flanagan, D. R. *J. Phys. Chem. B* **2006**, *110*, 17315.

(19) Tikhonovsky, A.; Kim, K.; Lee, S. K.; Nedoseykina, T.; Yang, M.; Song, S. A *Jpn. J. Appl. Phys. 1* **2006**, *45*, 8014.

(20) Okuyama, K.; Lenggoro, I. W. *Chem. Eng. Sci.* **2003**, *58*, 537.

(21) Panda, S.; Pratsinis, S. E. *Nanostruct. Mater.* **1995**, *5*, 755.

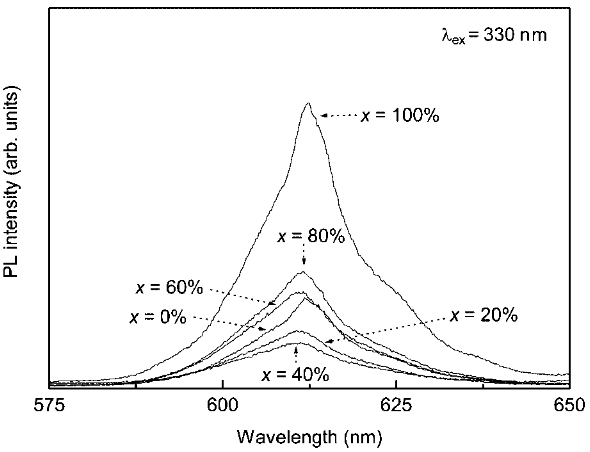

Figure 6. PL spectra of $Ca_xBa_{(1-x)}TiO_3:Pr^{3+}$ nanophosphors for various x monitored at an excitation wavelength of 330 nm.

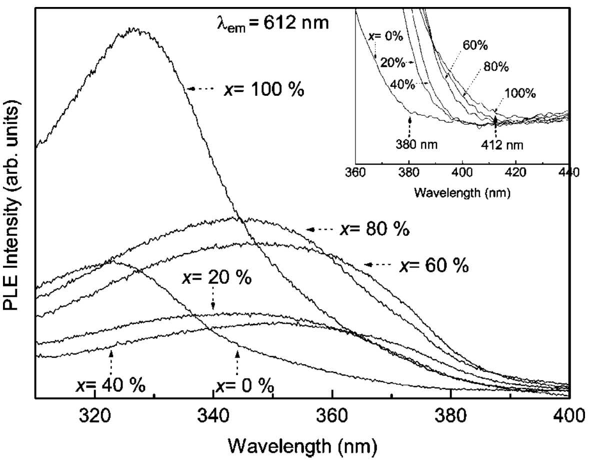

Figure 7. PLE spectra of $Ca_xBa_{(1-x)}TiO_3:Pr^{3+}$ nanophosphor monitored at an emission wavelength of 612 nm.

Consequently, the diffusion distance of the reactants in the FASP method is a few thousand-fold shorter than that of the solid-state method. This difference implies a faster reaction rate with FASP, resulting in complete substitution of Ba by Ca ions to produce a monophasic structure, as indicated in Figure 1. This result also proves that the biphasic $CaTiO_3$ and $BaTiO_3$ results from imperfect homogeneity due to incomplete diffusion of Ca into $BaTiO_3$.[12]

Having discovered the existence of a solid solution over the entire range of x, Pr^{3+} was doped into $Ca_xBa_{(1-x)}TiO_3$ to evaluate their photoluminescence properties as a function of x. Figure 6 shows the photoluminescence (PL) spectra of $Ca_xBa_{(1-x)}TiO_3:Pr^{3+}$ ($0\% \leq x \leq 100\%$) nanophosphors as a function of x under an excitation wavelength of 330 nm. A red luminescence emission in the Pr^{3+}-doped $Ca_xBa_{(1-x)}TiO_3$ nanophosphor originated from the intra 4f $^1D_2-^3H_4$ transition of Pr^{3+}, indicating that Pr^{3+} was effectively doped into the solid solution. The photoluminescence intensity diagram shows that the brightest light was emitted from the nanophosphor with $x = 100\%$ (pure $CaTiO_3$). The brightness gradually declined with x, until $x = 40\%$, and then it increased again when $x = 0\%$ (pure $BaTiO_3$). The emission characteristics of the rare earth phosphor are affected by the valence state of the dopants, the energy band structure, and the crystallinity of the host materials.[23-25] The correlation of the PL intensity to the bandgap (E_g) is mediated by the binding energy of excitons. A variation of the host matrix band gap (by variation of x in $Ca_xBa_{(1-x)}TiO_3$) would change the binding energy and, consequently, the PL intensity will vary accordingly. To relate PL intensity with the crystallinity of the host matrix, it is empirically found that the PL intensity of the phosphors is proportional to the crystallite size.[23,25] The crystallite sizes of nanophosphors were 10 nm, 9 nm, 7.6 nm, 6.9 nm, 20 nm, 20.2 nm, and 36 nm for $x = 0\%$, 20%, 40%, 60%, 80%, and 100%, respectively. The crystallite size of nanophosphors shows a consistent trend with the PL intensity as shown in Figure 6. PL emission wavelength peaks shifted insignificantly in the range of 610.6 to 612.4 nm. In addition, PL intensity is also affected by particles size, by which nanophosphors emit brighter emissions compared to that of bulk particles, as reported by Zhang et al.[26]

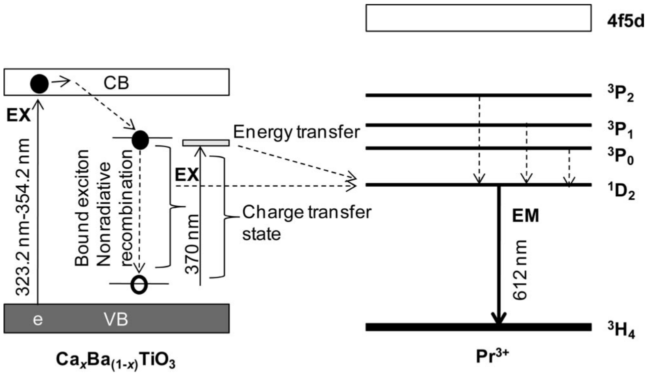

Figure 8. Simple model illustrating the energy-transfer and the red-emission processes in $Ca_xBa_{(1-x)}TiO_3:Pr^{3+}$.

The photoluminescence excitation (PLE) spectra of $Ca_xBa_{(1-x)}TiO_3:Pr^{3+}$ ($0\% \leq x \leq 100\%$) nanophosphors monitored at 612 nm is shown in Figure 7. A variation of x in $Ca_xBa_{(1-x)}TiO_3:Pr^{3+}$ nanophosphors is related to the variation of the onset position of PLE, as shown in the Figure 7 inset. As indicated in Table 1, the variation in x shifts the lattice parameters of $Ca_xBa_{(1-x)}TiO_3$ crystals, resulting in a variation of the host matrix band gap.[24,27] As a result, the onset PLE wavelength was varied from 380 to 412 nm by varying of x from 0% to 100%. In addition, the excitation wavelength peaks of red-emitting $Ca_xBa_{(1-x)}TiO_3:Pr^{3+}$ nanophosphors are 323.2, 336.8, 354.2, 345.6, 343.2, and 326.6 nm for $x = 0$, 20, 40, 60, 80, and 100%, respectively.

In the $ATiO_3$ (A = Ca, Ba, Sr) phosphor, the excitation of red luminescence was achieved through the conduction band (CB) state of the host matrix and transferred to the

---

(22) Kodas, T. T.; Smith, M. H. *Aerosol process of materials*; John Wiley & Sons, Inc.: New York, 1999.

(23) Lee, S. T.; Kitagawa, M.; Ichino, K.; Kobayashi, H. *Appl. Surf. Sci.* **1997**, *114*, 499.

(24) Shionoya, S.; Yen, W. M. *Phosphor Handbook*; CRC: Boca Raton, 1998.

(25) Wang, W. N.; Widiyastuti, W.; Ogi, T.; Lenggoro, I. W.; Okuyama, K. *Chem. Mater.* **2007**, *19*, 1723.

(26) Zhang, X.; Zhang, J.; Nie, Z.; Wang, M.; Ren, X. *Appl. Phys. Lett.* **2007**, *90*, 151911–1.

(27) Liu, X. M.; Jia, P. Y.; Lin, J.; Li, G. Z. *J. Appl. Phys.* **2006**, *99*, 124902–1.

emitting level of activator ions (Pr^{3+}). For $x = 100\%$ (pure $CaTiO_3$), the excitation spectrum of Pr^{3+}-doped nanoparticles ($CaTiO_3$:Pr^{3+}) shows a broadband with a peak at 326.6 nm and a small shoulder peak at approximately 370 nm. UV (326.6 nm) excitation generates the charge transfers of O(2p) → Ti(3d) and/or Pr^{3+}(4f) → Ti(3d) and the resulting electron−hole pairs imply the formation of bound excitons. Then, these excitons decay nonradiatively through a resonant or quasiresonant transfer to the 4f shell of Pr^{3+} ions.[4,5,26,27] A simple model illustrates both the energy-transfer and red-emission processes of Pr^{3+} in $Ca_xBa_{(1-x)}TiO_3$:Pr^{3+}, as shown in Figure 8. Finally, we have shown the existence of solid solution $Ca_xBa_{(1-x)}TiO_3$ for $x > 23\%$ and the Pr^{3+}-doped luminescence properties of the nanoparticles. This novel $Ca_xBa_{(1-x)}TiO_3$ system may provide a new area of research for the development of efficient red phosphors materials.

4. Conclusion

Monophasic $Ca_xBa_{(1-x)}TiO_3$ nanoparticles were obtained for all x concentrations using the FASP method. Biphasic structures of tetragonal $BaTiO_3$ and orthorhombic $CaTiO_3$ were not detected for $x > 23\%$, as indicated by the XRD spectra. A detailed characterization by STEM with EDS mapping showed that all components were perfectly distributed inside the nanoparticles. Supported by ICP analysis, the composition of the $Ca_xBa_{(1-x)}TiO_3$ nanoparticles was very similar to that of the precursor, indicating preservation of all components during fabrication. From the HR-TEM images and SAED spectra, it was concluded that $Ca_xBa_{(1-x)}TiO_3$ nanoparticles are spherical, nonagglomerated, and polycrystalline in nature. Pr^{3+}-doped $Ca_xBa_{(1-x)}TiO_3$ nanophosphors emit an intense red emission at a wavelength of 612 nm at an excitation wavelength of 330 nm. The variation of x in $Ca_xBa_{(1-x)}TiO_3$:Pr^{3+} varied the excitation wavelength peak over a range of 323.2 to 354.2 nm.

Acknowledgment. We thank Dr. Eishi Tanabe (Hiroshima Prefectural Institute of Industrial Science and Technology) for his assistance with the TEM. We also acknowledge the Ministry of Education, Culture, Sports, Science and Technology of Japan for providing a doctoral scholarship (D.H).

Supporting Information Available: (1) FE-SEM images of $Ca_xBa_{(1-x)}TiO_3$ ($x = 25\%$) prepared from different concentrations: (a) 0.05 M, (b) 0.075 M, (c) 0.1 M, and (d) 0.2 M. Insets: Geometric mean diameter and geometric standard deviation of the corresponding nanoparticles. (2) TEM, SAED spectra, and HR-TEM image of $Ca_xBa_{(1-x)}TiO_3$ ($x = 5\%$) nanoparticles. (3) Elemental analysis of $Ca_xBa_{(1-x)}TiO_3$ ($x = 20\%$) nanoparticle (PDF). This material is available free of charge via the Internet at http://pubs.acs.org.

CM802524E